

Preparation and measurement of three-qubit entanglement in a superconducting circuit

L. DiCarlo¹, M. D. Reed¹, L. Sun¹, B. R. Johnson¹, J. M. Chow¹, J. M. Gambetta², L. Frunzio¹, S. M. Girvin¹, M. H. Devoret¹ & R. J. Schoelkopf¹

Traditionally, quantum entanglement has been central to foundational discussions of quantum mechanics. The measurement of correlations between entangled particles can have results at odds with classical behaviour. These discrepancies grow exponentially with the number of entangled particles¹. With the ample experimental^{2–4} confirmation of quantum mechanical predictions, entanglement has evolved from a philosophical conundrum into a key resource for technologies such as quantum communication and computation⁵. Although entanglement in superconducting circuits has been limited so far to two qubits^{6–9}, the extension of entanglement to three, eight and ten qubits has been achieved among spins¹⁰, ions¹¹ and photons¹², respectively. A key question for solid-state quantum information processing is whether an engineered system could display the multi-qubit entanglement necessary for quantum error correction, which starts with tripartite entanglement. Here, using a circuit quantum electrodynamics architecture^{13,14}, we demonstrate deterministic production of three-qubit Greenberger–Horne–Zeilinger (GHZ) states¹⁵ with fidelity of 88 per cent, measured with quantum state tomography. Several entanglement witnesses detect genuine three-qubit entanglement by violating biseparable bounds by 830 ± 80 per cent. We demonstrate the first step of basic quantum error correction, namely the encoding of a logical qubit into a manifold of GHZ-like states using a repetition code. The integration of this encoding with decoding and error-correcting steps in a feedback loop will be the next step for quantum computing with integrated circuits.

With steady improvements in qubit coherence, control and read-out over a decade, superconducting quantum circuits¹⁶ have recently been used to show two important results in solid-state two-qubit entanglement. The first is the violation of a Bell inequality without a detection loophole, realized with phase qubits by minimizing crosstalk between high-fidelity individual qubit read-outs⁵. The second is the realization of simple quantum algorithms⁷, achieved through improved two-qubit gates and coherence in circuit quantum electrodynamics (cQED). With entanglement between two engineered qubits firmly established, the next challenge is to scale up entanglement to the threshold at which quantum error correction becomes possible. The simplest schemes rely on three-qubit entanglement (3QE) to protect against either random single-qubit flips or quantum phase errors⁵. An algorithmic approach, pursued here, builds up 3QE with a properly compiled sequence of single- and two-qubit gates. A more physical approach exploits effective three-body interactions, as used in an independent and parallel effort¹⁷.

Our superconducting chip (Fig. 1a) consists of four transmon qubits (Q_1 to Q_4 , anticlockwise from top right) inside a transmission-line cavity that couples them²⁰, isolates them from the electromagnetic environment²¹ and allows their joint read-out^{9,22,23}. As in its two-qubit predecessor^{7,9}, in our chip qubit control is achieved with a combination of resonant microwave drives realizing single-qubit x and y rotations and flux pulses individually tuning the qubit transition

frequencies on nanosecond timescales. Flux pulses inducing small frequency excursions ($\lesssim 100$ MHz) realize z rotations. Stronger pulses (~ 650 MHz excursions) drive specific computational levels into resonance with non-computational ones (involving second-excited states of Q_2 and Q_3) to realize conditional-phase gates^{7,24} (C-Phase) that

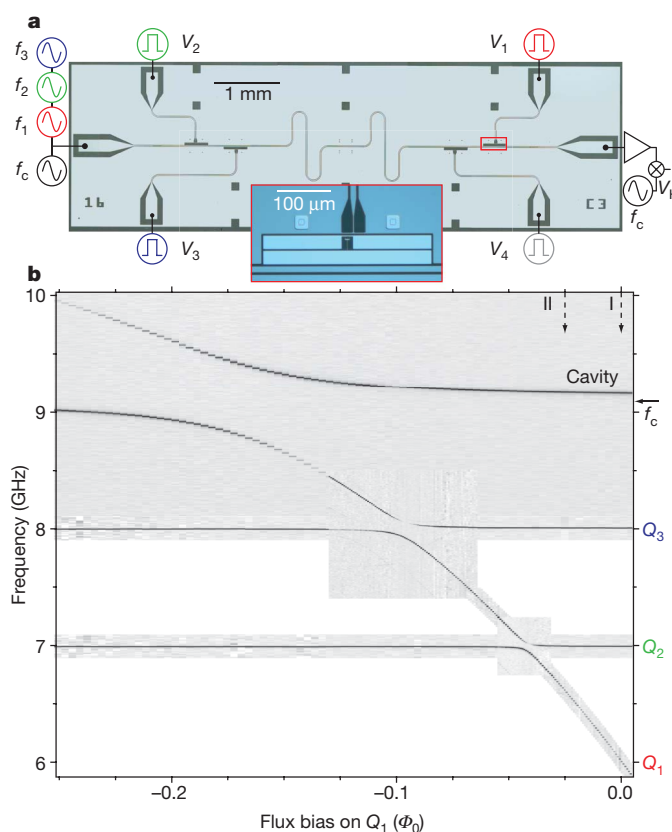


Figure 1 | Four-qubit cQED processor, and spectroscopic characterization.

a, Micrograph of a six-port superconducting device with four transmon qubits (Q_1 (inset) to Q_4) inside a meandering coplanar waveguide resonator. Local flux-bias lines allow qubit tuning on nanosecond timescales with room-temperature voltages V_i . Microwave pulses at qubit transition frequencies f_1 , f_2 and f_3 realize single-qubit x and y rotations in 8 ns. Q_4 (operational but unused) is biased at its maximal frequency (12.271 GHz) to minimize its interaction with the qubits used. Pulsed measurement of cavity homodyne voltage V_H (at the bare cavity frequency, $f_c = 9.070$ GHz) allows joint qubit read-out. A detailed schematic of the measurement set-up is shown in Supplementary Fig. 2. **b**, Greyscale images of cavity transmission and qubit spectroscopy versus local tuning of Q_1 show avoided crossings with Q_2 , with Q_3 and with the cavity. Points I and II are two of three operating points (Fig. 2 shows point III). Single-qubit gates and joint read-out are performed at point I. C-Phase gates between Q_1 and Q_2 are achieved by flux pulsing to point II.

¹Departments of Physics and Applied Physics, Yale University, New Haven, Connecticut 06511, USA. ²Department of Physics and Astronomy and Institute for Quantum Computing, University of Waterloo, Waterloo, Ontario N2L 3G1, Canada.

entangle nearest neighbours in frequency, as discussed below. The read-out exploits qubit-state-dependent cavity transmission to gain direct access to multi-qubit correlations, facilitating full tomography of the qubit register and entanglement witnessing. We emphasize that doubling the number of coupled qubits has been achieved without significantly increasing the complexity of circuit design, sample fabrication or experimental calibration, demonstrating the power of a quantum bus architecture.

The spectrum of single excitations of the three used qubits (Q_1 to Q_3) and the cavity reveals key features of the generalized Tavis–Cummings Hamiltonian describing the system and allows extraction of its parameters (Methods Summary). Spectroscopy as a function of local flux tuning of Q_1 (Fig. 1b) shows exactly three avoided crossings: J crossings²⁰ with Q_2 and with Q_3 , and the vacuum Rabi splitting¹³ with the cavity near its bare frequency, $f_c = 9.070$ GHz. To the resolution of all spectroscopy performed, the spectrum is free from spurious avoided crossings, which is a critical requirement for pulsed excursions of qubit transition frequencies. We choose point I (where $f_1 = 6.000 \pm 0.002$ GHz, $f_2 = 7.000 \pm 0.002$ GHz and $f_3 = 8.000 \pm 0.002$ GHz; see Fig. 1b) for all single-qubit rotations and for read-out. Here, the qubits are sufficiently detuned in frequency from their nearest neighbours to make their interaction small, yet close enough to the cavity to reach the strong-dispersive regime of cQED²⁵.

Two-qubit C-Phase gates generate entanglement in the computational basis $\{|abc\rangle \mid a, b, c \in \{0, 1\}\}$ ($|abc\rangle$ denotes excitation level a on Q_1 , b on Q_2 and c on Q_3). A C-Phase gate, denoted $cP_{a,b}^{j,j}$, adds a phase shift of π to the quantum amplitudes of the two basis states with excitation levels a in Q_i and b in Q_j , leaving the quantum amplitudes of the remaining six basis states unchanged. We realize C-Phase gates between nearest neighbours in frequency (between Q_1 and Q_2 , and between Q_2 and Q_3) by direct extension of the protocol proposed for phase qubits in ref. 24, in which a full coherent oscillation between computational and non-computational states yields the desired π phase shift. The primitive interaction for C-Phase gates between Q_2 and Q_3 is shown with two-tone spectroscopy and time-domain data in Fig. 2. (See Supplementary Fig. 1 for a similar characterization for Q_1 and Q_2 .) At point III (Fig. 2), the computational level $|011\rangle$ becomes resonant with the non-computational level $|002\rangle$. The cavity-mediated interaction between these levels produces an avoided crossing of 86 MHz. An analogous avoided crossing takes place simultaneously in the three-excitation manifold, between $|111\rangle$ and $|102\rangle$. A coherent oscillation between these computational and non-computational levels is started by pulsing non-adiabatically into point III. A full period is completed in 12 ns (Fig. 2, inset), returning all the quantum amplitude to the computational level with an additional phase of π . The two-qubit gate time is nearly half that of our previous implementation, which used the avoided crossing adiabatically⁷. To complete $cP_{1,1}^{2,3}$, the single-qubit dynamical phase acquired by Q_2 during the flux pulse (and also by Q_1 and Q_3 through residual flux cross-talk) is cancelled using a calibrated z rotation (Supplementary Fig. 3). The other three C-Phase gates between Q_2 and Q_3 can be produced with additional single-qubit z gates applied to one or both qubits⁷.

To detect the entanglement produced with C-Phase gates, we use a high-fidelity three-qubit joint read-out presented in a related publication²³. Read-out was previously performed^{7,9,22} with a pulsed measurement of cavity transmission in linear response (~ 1 photon mean occupation) at the dispersively shifted cavity frequency corresponding to $|000\rangle$. Here we instead drive at f_c and with a 50,000-fold larger incident power. This approach increases the single-shot read-out fidelity in this device from $\sim 5\%$ to 61%. The physical mechanism allowing this improvement is due to the Jaynes–Cummings interaction: as its excitation number increases, the cavity is pulled from its dispersively shifted frequency towards f_c and its anharmonicity decreases²⁶. A sufficiently strong drive at f_c excites the cavity high enough that it responds harmonically, yielding near-unit transmission. Crucially, because of the dependence of cavity anharmonicity and dispersive shift

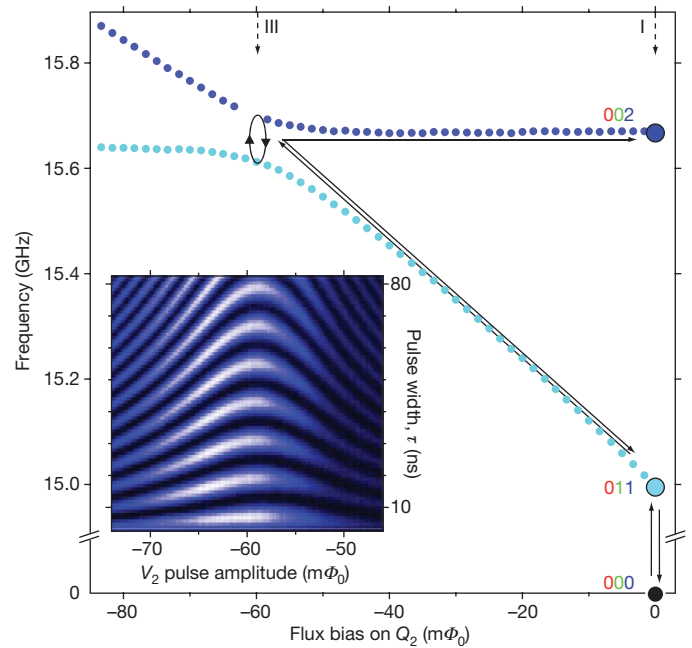


Figure 2 | Frequency- and time-domain characterization of two-qubit-gate primitive. Two-tone spectroscopy¹⁹ of computational level $|011\rangle$ and non-computational level $|002\rangle$ through their avoided crossing (86-MHz splitting) at point III. This crossing (and its $|111\rangle \leftrightarrow |102\rangle$ analogue in the three-excitation manifold) is the primitive for C-Phase gates between Q_2 and Q_3 (ref. 24). The gate is realized with a sudden flux pulse into point III. While the pulse is on, the quantum amplitude initially in $|011\rangle$ is coherently exchanged with $|002\rangle$. The pulse is turned off after one full period, at which time all quantum amplitude returns to $|011\rangle$, but with an additional phase of π . Inset, time-domain characterization of the avoided crossing using the sequence outlined by the arrows in the main panel. Starting from $|000\rangle$, simultaneous π -pulses on Q_2 and Q_3 populate $|011\rangle$. A V_2 pulse of duration τ is next applied. Simultaneous π -pulses then transfer the final quantum amplitude in $|011\rangle$ to $|000\rangle$ to maximize read-out contrast. This characterization gives a calibration of the optimal flux-pulse duration, in this case 12 ns.

on qubit state, the drive power needed is qubit-state dependent. We adjust the incident power so that the cavity becomes excited for all register states except $|000\rangle$. If this selectivity were perfect, the measurement would be projective on $|000\rangle$, yielding the ensemble average $\langle V_H \rangle \propto \sum_{A,B,C \in \{I,Z\}} \langle A^{(1)} B^{(2)} C^{(3)} \rangle$. Here I is the identity, Z is the Pauli Z operator⁵ and $A^{(i)}$ acts on Q_i (henceforth this order of operators is respected and superscripts are removed for notational simplicity). False positives and negatives introduce weighting coefficients, β_{ABC} . The similar magnitudes of the calibrated coefficients (Methods Summary) translate into a sensitivity of joint read-out to two- and three-qubit correlations comparable to the sensitivity to single-qubit polarizations⁹.

We use this single-channel measurement with direct access to correlations to perform state tomography of the register. To reconstruct the three-qubit density matrix, ρ , we find the coefficients of its expansion in the Pauli operator basis⁵:

$$\rho = \frac{1}{8} \sum_{A,B,C \in \{I,X,Y,Z\}} \langle ABC \rangle ABC \quad (1)$$

Here $\langle III \rangle = 1$, and X and Y are the Pauli X and Y operators⁵. This is achieved by prefixing the read-out pulse with 63 different sets of single-qubit rotations (Methods Summary).

With fast C-Phase gates and high-fidelity read-out in place, we now demonstrate multi-qubit entanglement. Gate sequences generating two- and three-qubit entanglement are shown in Fig. 3. A simple sequence⁷ using one C-Phase transforms the ground state $|000\rangle$ (an unentangled, or separable, state) into a Bell triplet $|0\rangle \otimes (|00\rangle + |11\rangle)/\sqrt{2}$

$\sqrt{2}$ with Q_2 and Q_3 maximally entangled (Fig. 3b). Mirroring this sequence so that Q_1 undergoes the same operations as Q_3 (Fig. 3c) produces the GHZ state, $|\text{GHZ}\rangle = (|000\rangle + |111\rangle)/\sqrt{2}$, which is a maximally entangled state of three qubits. We have implemented these sequences (see Supplementary Fig. 3 for the actual microwave and flux pulses realizing the GHZ sequence) and performed tomography of their outputs. We visualize the reconstructed ρ in each case using a bar chart of the Pauli set \mathbf{P} , consisting of the expectation values of the 63 non-trivial Pauli operators. Although it contains the same information as the more conventional ‘cityscape’ visualization of ρ (Supplementary Fig. 4), this bar chart reveals more clearly the polarization of each qubit and the correlations present between qubits. The experimental sets \mathbf{P} in Fig. 3d–f closely match the delineated Pauli set, \mathbf{P}_t , of the targeted ground state, the Bell triplet and the GHZ state, respectively. We quantify this similarity using fidelity to the target state $|\psi_t\rangle$, $F = \langle \psi_t | \rho | \psi_t \rangle = \mathbf{P} \cdot \mathbf{P}_t / 8$, finding $F = 99\%$, 94% and 88% , respectively.

To make definitive statements about the presence of genuine 3QE in Fig. 3f, we make use of fidelity to GHZ states as an entanglement witness²⁷. The maximal fidelity of any biseparable state (a state with no more than two qubits entangled) to a GHZ state is 50%. Any greater fidelity thus witnesses genuine 3QE. There are two types of 3QE, W and GHZ, with the GHZ class encompassing the W class. Fidelity also witnesses strictly GHZ-type 3QE, the kind useful for quantum error correction, because $F \leq 75\%$ for all W-class states. An unverified production of W-class entanglement in cQED was investigated previously²⁸ by tripartite interaction between two phase qubits and a resonant cavity. The 88% fidelity to $|\text{GHZ}\rangle$ of the Pauli set in Fig. 3f is a demonstration of not only genuine but also strictly GHZ-type 3QE in an engineered solid-state system.

This production of 3QE is a first step towards basic quantum error correction. The sequence producing the GHZ state (Fig. 3c) can be viewed as the application of a repetition code (Fig. 4a) to a superposition state, $(|0\rangle + |1\rangle)/\sqrt{2}$, of Q_2 . The repetition code is the encoding step of the bit-flip error-correction scheme³, mapping a logical qubit state $\alpha|0\rangle + \beta|1\rangle$ onto the state $\alpha|000\rangle + \beta|111\rangle$ of three physical qubits. We have applied this code to other maximal superpositions of Q_2 by varying the azimuthal angle, ϕ , of its initial $\pi/2$ rotation (Fig. 4a). At each ϕ , the code targets the state $|\text{GHZ}_\phi\rangle = (|000\rangle - ie^{i\phi}|111\rangle)/\sqrt{2}$. The fidelity to $|\text{GHZ}_\phi\rangle$ is $87 \pm 1\%$ throughout (Fig. 4b), witnessing GHZ-class 3QE at every ϕ . A master equation simulation suggests that this uniform fidelity is mostly limited by qubit relaxation during the 81-ns pulse sequence. A model incorporating low-frequency and possibly non-local dephasing seems to be necessary to account for the small extra infidelity, and remains for future work.

It is possible to detect 3QE with linear witnesses requiring measurement of fewer elements of the Pauli set than the fidelity to a GHZ state. For example, the Mermin sums¹ $\mathcal{M}_{S1} = \langle XXX \rangle - \langle YYX \rangle - \langle YXY \rangle - \langle XYY \rangle$ and $\mathcal{M}_{S2} = -\langle YYY \rangle + \langle XXY \rangle + \langle XYX \rangle + \langle YXX \rangle$ satisfy $|\mathcal{M}_{S1,2}| \leq 2$ for all biseparable states²⁹. Figure 4c shows that at least one of these sums detects 3QE at each ϕ . We note that $|\mathcal{M}_{S1,2}| \leq 2$ is also a local-hidden-variable (LHV) bound¹. Although the maximal absolute value measured, 3.4 ± 0.1 , exceeds this bound by 14 standard deviations, the presence of locality and detection loopholes³⁰ in our system precludes a complete refutation of local realism.

One drawback of the Mermin sums as witnesses of 3QE is that the biseparable range overlaps significantly with the quantum range for three qubits, $|\mathcal{M}_{S1,2}| \leq 4$. Nonlinear entanglement witnesses can compress the biseparable bounds relative to the quantum bounds, effectively

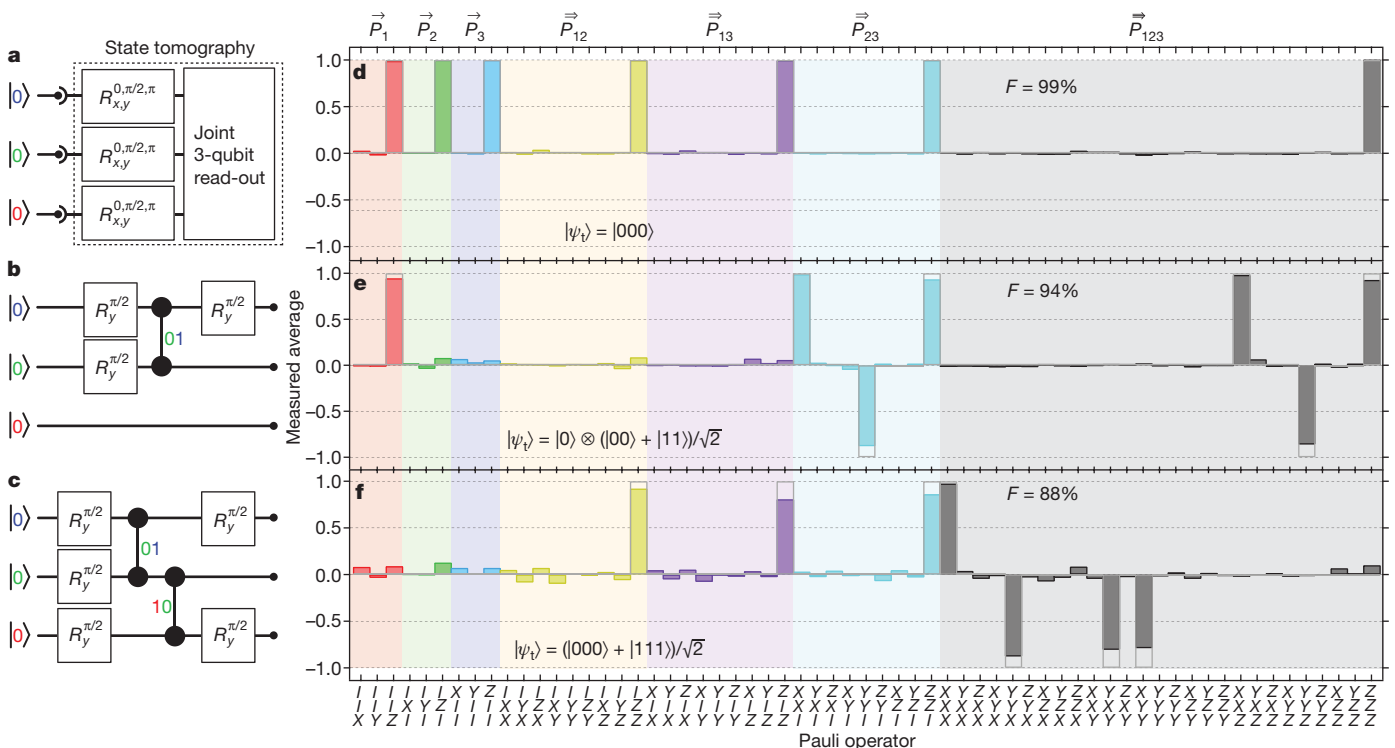


Figure 3 | Building 3QE with two two-qubit gates. **a–c**, Gate sequences producing states with increasing numbers of entangled qubits: the ground state (no entanglement; **a**), a Bell triplet (Q_2 and Q_3 , entangled; **b**) and the GHZ state (3QE, **c**). Vertical lines terminating in solid circles represent C-Phase gates. The coloured two-bit number next to each indicates the computational basis states that acquire the phase π . The state tomography sequence shown in **a** is also applied in **b** and **c**. **d–f**, Reconstructed density matrices of the sequence outputs, visualized with a bar chart of the Pauli set \mathbf{P} . Colours emphasize the seven

subsets of \mathbf{P} (Bloch vectors ($\vec{P}_1, \vec{P}_2, \vec{P}_3$), two-qubit correlations ($\vec{P}_{12}, \vec{P}_{13}, \vec{P}_{23}$) and three-qubit correlations (\vec{P}_{123})). The Pauli set of the target state $|\psi_t\rangle$, \mathbf{P}_t , is superposed (open bars). The sets \mathbf{P}_t have seven non-zero and full-magnitude components because they represent stabilizer states⁵. For the GHZ state, they appear exclusively in the correlations, which is a hallmark of maximal 3QE. The experimental sets \mathbf{P} closely match \mathbf{P}_t in the three cases, with fidelities $F = \langle \psi_t | \rho | \psi_t \rangle = \mathbf{P} \cdot \mathbf{P}_t / 8$ of 99%, 94% and 88%.

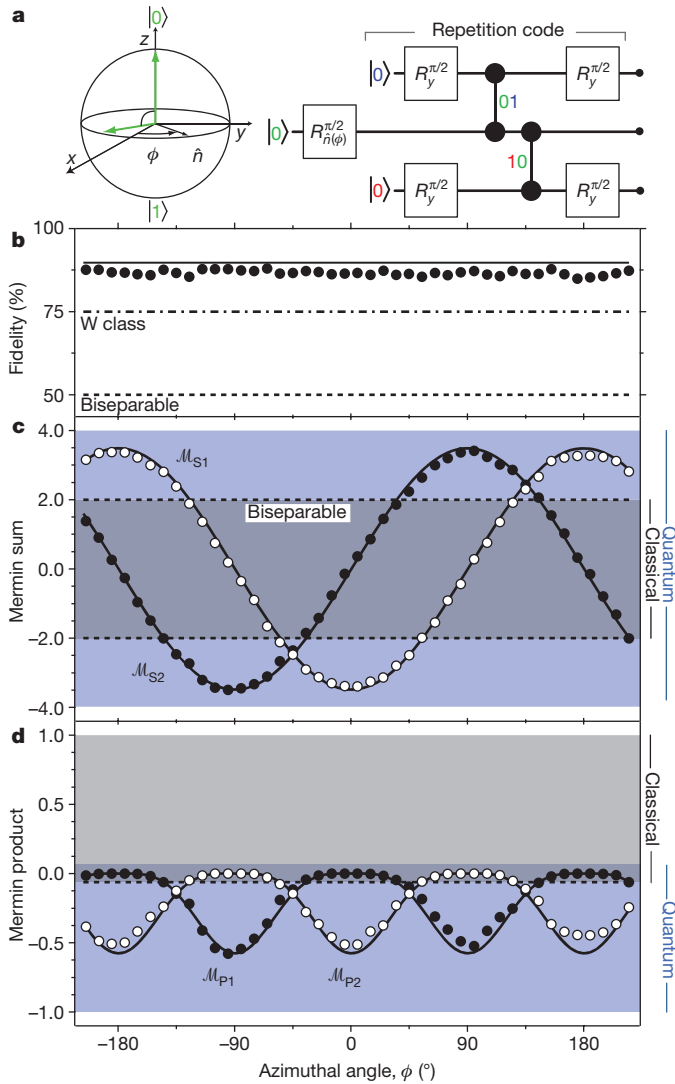


Figure 4 | Witnessing of 3QE using fidelity and Mermin inequalities. **a**, Gate sequence mapping superpositions $(|0\rangle - ie^{i\phi}|1\rangle)/\sqrt{2}$ of Q_2 into GHZ states $|\text{GHZ}_\phi\rangle = (|000\rangle - ie^{i\phi}|111\rangle)/\sqrt{2}$ using a repetition code. **b**, Fidelity $F = \langle \text{GHZ}_\phi | \rho | \text{GHZ}_\phi \rangle$ as a function of the azimuthal angle, ϕ , of the initial $\pi/2$ rotation on Q_2 , averaging 87%. Biseparable and W-class bounds are amply exceeded, witnessing stringent GHZ-class 3QE. **c**, Evolution of the Mermin sums $\mathcal{M}_{S1} = \langle XXX \rangle - \langle YYY \rangle - \langle YXY \rangle - \langle XYY \rangle$ and $\mathcal{M}_{S2} = -\langle YYY \rangle + \langle XXY \rangle + \langle XYX \rangle + \langle YXX \rangle$. Biseparable bounds are broken by at least one sum at each ϕ , witnessing 3QE. The extremal measured value, 3.4 ± 0.1 , largely exceeds the LHV bound (grey shading) but remains inside the range allowed by quantum mechanics assuming three qubits (blue shading). **d**, Evolution of the Mermin products $\mathcal{M}_{P1} = \langle XXX \rangle \langle YYY \rangle \langle YXY \rangle \langle XYY \rangle$ and $\mathcal{M}_{P2} = \langle YYY \rangle \langle XXY \rangle \langle XYX \rangle \langle YXX \rangle$. The minimum value measured, of -0.52 ± 0.05 , violates the negative biseparable (also LHV) bound, $\mathcal{M}_{P1,2} \geq -1/16$, by $830 \pm 80\%$. Solid curves in the three panels correspond to a master equation simulation that includes qubit relaxation during the pulse sequence.

magnifying non-trivial three-qubit correlations. As a specific example, we here introduce the Mermin products $\mathcal{M}_{P1} = \langle XXX \rangle \langle YYY \rangle \langle YXY \rangle \langle XYY \rangle$ and $\mathcal{M}_{P2} = \langle YYY \rangle \langle XXY \rangle \langle XYX \rangle \langle YXX \rangle$, whose various bounds we have explored numerically. As indicated, biseparable states satisfy $-1/16 \leq \mathcal{M}_{P1,2} \leq 1/64$, which is a range small in comparison with the quantum range for three qubits, $-1 \leq \mathcal{M}_{P1,2} \leq 1/16$. The LHV range for Mermin products is $-1/16 \leq \mathcal{M}_{P1,2} \leq 1$. We note that although the LHV range for Mermin sums is fully inside the range allowed by quantum mechanics, the two ranges largely separate for products, leaving only a narrow region of compatibility, $|\mathcal{M}_{P1,2}| \leq 1/16$. The measured Mermin products (Fig. 4d) reach a minimum value of -0.52 ± 0.05 ,

which exceeds the negative biseparable (also LHV) bound by $830 \pm 80\%$. The experimental $\mathcal{M}_{P1,2}$ values fall largely outside the compatibility region, and remain fully within the quantum bounds.

This demonstration of 3QE in an integrated circuit allows the exploration of quantum error correction in the solid state. We have realized the first step of the simple bit-flip code, namely using a repetition code to map a superposition state of one logical qubit into an entangled state of three physical qubits. Future research will focus on the development of an error-syndrome detecting circuit with the aim of closing the error-correction feedback loop.

METHODS SUMMARY

Hamiltonian parameters. The Tavis–Cummings Hamiltonian generalized to four transmons is

$$H = \hbar\omega_c a^\dagger a + \hbar \sum_{q=1}^4 \left(\sum_{j=0}^N \omega_{0j}^{(q)} |j\rangle_q \langle j|_q + (a + a^\dagger) \sum_{j,k=0}^N g_{jk}^{(q)} |j\rangle_q \langle k|_q \right)$$

Here \hbar is Planck's constant (h) divided by 2π , ω_c is the bare cavity frequency, $\omega_{0j}^{(q)}$ is the transition frequency for transmon q from ground to excited state j , and $g_{jk}^{(q)} = g_q n_{jk}$, with g_q a bare qubit-cavity coupling and n_{jk} a coupling matrix element. Both $\omega_{0j}^{(q)}$ and n_{jk} are functions¹⁸ of transmon charging (E_{Cq}) and Josephson (E_{Jq}) energies. Flux control enters through $E_{Jq} = E_{Jq}^{\max} |\cos(\pi\Phi_q/\Phi_0)|$, with Φ_q the flux through the transmon superconducting-interference-device loop, and a linear flux-voltage relation, $\Phi_q = \sum_{i=1}^4 \alpha_{qi} V_i + \Phi_{q,0}$ capturing cross-talk (α_{qi}) and offsets ($\Phi_{q,0}$; Φ_0 is the flux quantum). Cross-talk ($\lesssim 40\%$) resulting from ground-plane return currents is corrected by orthogonalization. Fitting numerical diagonalizations of H (truncated to $N = 4$ transmon levels and four cavity photons) to the spectroscopy and transmission data shown (Figs 1b and 2 and Supplementary Fig. 2) and to similar data (not shown) as a function of flux bias on Q_2 to Q_4 gives $\omega_c/2\pi = 9.070$ GHz; $E_{Jq}^{\max}/h = 42$ GHz (Q_1), 29 GHz (Q_2), 47 GHz (Q_3), 57 GHz (Q_4); $g/2\pi \approx 220$ MHz; and $E_{Cq}/h \approx 330$ MHz.

Coherence times. Relaxation (T_1) and dephasing (T_2^*) times of Q_1 to Q_3 were measured using sliding π -pulse and Ramsey experiments¹⁹. At point I, relaxation times $T_1 = 1.2$ μ s (Q_1), 1.0 μ s (Q_2) and 0.6 μ s (Q_3) are consistent with relaxation by means of the Purcell effect²¹ and non-radiative loss with quality factor $\sim 55,000$. Dephasing times $T_2^* = 0.3$ μ s, 0.6 μ s and 0.5 μ s are consistent with $1/f$ flux noise of $\sim 10^{-5}$ Φ_0 Hz $^{-1/2}$ at 1 Hz. The cavity linewidth is $\kappa/2\pi = 2.4$ MHz.

Calibration of joint read-out. The coefficients β in the measurement operator are calibrated in every tomography run by applying joint read-out to the eight computational states, prepared using π -pulses. For example, the ensemble-averaged read-out of $|101\rangle$ gives $\langle V_H \rangle = \beta_{111} - \beta_{211} - \beta_{121} - \beta_{112} - \beta_{221} + \beta_{212} - \beta_{122} + \beta_{222}$. These calibration measurements provide eight linearly independent combinations of the coefficients. Typical values obtained by matrix inversion are $\beta_{211} = 2.2$ mV, $\beta_{121} = 3.1$ mV, $\beta_{112} = 3.2$ mV, $\beta_{221} = 1.9$ mV, $\beta_{212} = 2.0$ mV, $\beta_{122} = 2.9$ mV and $\beta_{222} = 1.7$ mV. Their similar magnitudes imply comparable sensitivity to two- and three-qubit correlations (terms with two and three Z terms, respectively) relative to single-qubit polarizations⁹ (terms with one Z).

State tomography. The sets of rotations preceding read-out are all combinations of I , R_x^π , $R_x^{\pi/2}$ and $R_y^{\pi/2}$ on the three qubits (except $R_x^\pi \otimes R_x^\pi \otimes R_x^\pi$). Respectively, these rotations on Q_i transform the expression for $\langle V_H \rangle$ like so: $Z^{(i)} \rightarrow Z^{(i)}$, $-Z^{(i)}$, $Y^{(i)}$ and $-X^{(i)}$. Repeating 10^5 state preparations and single-shot measurements for each set mitigates projection noise to $< 1\%$. The non-trivial coefficients in equation (1) are obtained from the 63 $\langle V_H \rangle$ values by matrix inversion and without maximum-likelihood estimation⁹.

Received 20 April; accepted 9 August 2010.

- Mermin, N. D. Extreme quantum entanglement in a superposition of macroscopically distinct states. *Phys. Rev. Lett.* **65**, 1838–1840 (1990).
- Aspect, A., Dalibard, J. & Roger, G. Experimental test of Bell's inequalities using time-varying analyzers. *Phys. Rev. Lett.* **49**, 1804–1807 (1982).
- Pan, J.-W., Bouwmeester, D., Danielli, M., Weinfurter, H. & Zeilinger, A. Experimental test of quantum nonlocality in three-photon Greenberger–Horne–Zeilinger entanglement. *Nature* **403**, 515–519 (2000).
- Zhao, Z. *et al.* Experimental violation of local realism by four-photon Greenberger–Horne–Zeilinger entanglement. *Phys. Rev. Lett.* **91**, 180401 (2003).
- Nielsen, M. A. & Chuang, I. L. *Quantum Computation and Quantum Information* (Cambridge Univ. Press, 2000).
- Steffen, M. *et al.* Measurement of the entanglement of two superconducting qubits via state tomography. *Science* **313**, 1423–1425 (2006).
- DiCarlo, L. *et al.* Demonstration of two-qubit algorithms with a superconducting quantum processor. *Nature* **460**, 240–244 (2009).

8. Ansmann, M. *et al.* Violation of Bell's inequality in Josephson phase qubits. *Nature* **461**, 504–506 (2009).
9. Chow, J. M. *et al.* Detecting highly entangled states with a joint qubit readout. *Phys. Rev. A* **81**, 062325 (2010).
10. Neumann, P. *et al.* Multipartite entanglement among single spins in diamond. *Science* **320**, 1326–1329 (2008).
11. Häffner, H. *et al.* Scalable multiparticle entanglement of trapped ions. *Nature* **438**, 643–646 (2005).
12. Gao, W.-B. *et al.* Experimental demonstration of a hyper-entangled ten-qubit Schrödinger cat state. *Nature Phys.* **6**, 331–335 (2010).
13. Wallraff, A. *et al.* Strong coupling of a single photon to a superconducting qubit using circuit quantum electrodynamics. *Nature* **431**, 162–167 (2004).
14. Blais, A., Huang, R.-S., Wallraff, A., Girvin, S. M. & Schoelkopf, R. J. Cavity quantum electrodynamics for superconducting electrical circuits: an architecture for quantum computation. *Phys. Rev. A* **69**, 062320 (2004).
15. Greenberger, D. M., Horne, M. A. & Zeilinger, A. in *Bell's Theorem, Quantum Theory and Conceptions of the Universe* (ed. Kafatos, M.) 69–72 (Kluwer Academic, 1989).
16. Clarke, J. & Wilhelm, F. K. Superconducting quantum bits. *Nature* **453**, 1031–1042 (2008).
17. Neeley, M. *et al.* Generation of three-qubit entangled states using superconducting phase qubits. *Nature* doi:10.1038/nature09418 (this issue).
18. Koch, J. *et al.* Charge-insensitive qubit design derived from the Cooper pair box. *Phys. Rev. A* **76**, 042319 (2007).
19. Schreier, J. A. *et al.* Suppressing charge noise decoherence in superconducting charge qubits. *Phys. Rev. B* **77**, 180502(R) (2008).
20. Majer, J. *et al.* Coupling superconducting qubits via a cavity bus. *Nature* **449**, 443–447 (2007).
21. Houck, A. A. *et al.* Controlling the spontaneous emission of a superconducting transmon qubit. *Phys. Rev. Lett.* **101**, 080502 (2008).
22. Filipp, S. *et al.* Two-qubit state tomography using a joint dispersive readout. *Phys. Rev. Lett.* **102**, 200402 (2009).
23. Reed, M. D. *et al.* High-fidelity readout in circuit quantum electrodynamics using the Jaynes-Cummings nonlinearity. *Phys. Rev. Lett.* (in the press); preprint at (<http://arxiv.org/abs/1004.4323>) (2010).
24. Strauch, F. W. *et al.* Quantum logic gates for coupled superconducting phase qubits. *Phys. Rev. Lett.* **91**, 167005 (2003).
25. Schuster, D. I. *et al.* Resolving photon number states in a superconducting circuit. *Nature* **445**, 515–518 (2007).
26. Bishop, L. S., Ginossar, E. & Girvin, S. M. Response of the strongly-driven Jaynes-Cummings oscillator. *Phys. Rev. Lett.* **105**, 100505 (2010).
27. Acín, A., Bruß, D., Lewenstein, M. & Sanpera, A. Classification of mixed three-qubit states. *Phys. Rev. Lett.* **87**, 040401 (2001).
28. Altomare, F. *et al.* Tripartite interactions between two phase qubits and a resonant cavity. Preprint at (<http://arxiv.org/abs/1004.0026>) (2010).
29. Tóth, G. & Gühne, O. Entanglement detection in the stabilizer formalism. *Phys. Rev. A* **72**, 022340 (2005).
30. Kwiat, P. G., Eberhard, P. H., Steinberg, A. M. & Chiao, R. Y. Proposal for a loophole-free Bell inequality experiment. *Phys. Rev. A* **49**, 3209–3220 (1994).

Supplementary Information is linked to the online version of the paper at www.nature.com/nature.

Acknowledgements We thank M. Brink for experimental contributions, and L. S. Bishop, E. Ginossar, O. Gühne, C. Rigetti, D. I. Schuster and J. Siewert for discussions. We acknowledge support from LPS/NSA under ARO contract W911NF-05-1-0365, from IARPA under ARO contract W911NF-09-1-0369 and from the NSF under grants DMR-0653377 and DMR-0603369. Additional support was provided by CNR-Istituto di Cibernetica, Pozzuoli, Italy (L.F.), and by CIFAR, MITACS, MRI and NSERC (J.M.G.). All statements of fact, opinion or conclusions contained herein are those of the authors and should not be construed as representing the official views or policies of the US Government.

Author Contributions L.D.C., M.D.R. and L.S. carried out measurements and data analysis. B.R.J. and J.M.C. provided further experimental contributions. J.M.G. provided theory support. L.F., L.D.C. and L.S. fabricated devices. L.D.C. and M.H.D. wrote the manuscript, with feedback from all authors. S.M.G., M.H.D. and R.J.S. designed and supervised the project.

Author Information Reprints and permissions information is available at www.nature.com/reprints. The authors declare no competing financial interests. Readers are welcome to comment on the online version of this article at www.nature.com/nature. Correspondence and requests for materials should be addressed to L.D.C. (leonardo.dicarlo@yale.edu) or R.J.S. (robert.schoelkopf@yale.edu).